RSC Advances

PAPER

View Article Online
View Journal | View Issue

Cite this: *RSC Adv.*, 2021, **11**, 34079

Improving the capacity of zinc-ion batteries through composite defect engineering†

Juhua Huang, Yuning Cao, Ming Cao * and Jiajie Zhong

Received 29th July 2021
Accepted 12th October 2021

DOI: 10.1039/d1ra05775h

rsc.li/rsc-advances

Aqueous zinc-ion batteries (ZIB) are favored because of their low cost and high safety. However, as the most widely used cathodes, the rate performance and long-term cycle performance of manganese-based oxides are very worrying, which greatly affects their commercialization. Here, MnO_2 with composite defects of cation doping and oxygen vacancies was synthesized for the first time. Cation doping promoted the diffusion and transport of H^+ and oxygen vacancies weakened the zinc–oxygen bond, allowing more electrons to be added to the charge and discharge process. The combination of these makes α-MnO_2 obtain a specific capacity of up to 346 mA h g^{-1}. This inspired us to use different combinations of defect engineering strategies on the materials which can be implemented as a potential method to improve performance for the modification of ZIB cathode materials, such as cation vacancies and anion doping.

Introduction

Energy is an important and urgent problem for human survival and social development today. With the depletion of fossil resources such as coal and petroleum, renewable energy has attracted worldwide attention.[1] Among them, battery technology is widely used in the fields of automobiles and communications. Thanks to the unremitting efforts of researchers, in addition to mature lithium battery technology,[2] other battery systems have been rapidly developed, such as lithium oxygen batteries,[3] sodium ion batteries,[4] and potassium ion batteries.[5] Among the battery systems that have been reported, water-based batteries have received extensive attention and research due to their higher power density, higher safety, and lower cost.[6] The most reported water-based batteries may be the water-based zinc ion batteries (ZIBs). This is because metallic zinc not only has a theoretical specific capacity of up to 820 mA h g^{-1}, but also has a low cost and is harmless and abundant.[7] Although these advantages of zinc-ion batteries are attractive enough, the cathode material severely restricts the development of zinc-ion batteries.

So far, the most studied cathode materials are manganese-based materials,[8] vanadium-based materials,[9] Prussian blue and its analogues,[10] and metal sulfides.[11] Among these materials, manganese-based materials are favored because of their high specific capacity, low cost, and polymorphism. However, in actual research, the electrochemical properties of manganese-based materials are not satisfactory, such as their capacity and rate performance.[12] One of the most noticeable is the poor cycle performance, so that it is necessary to add $MnSO_4$ to the electrolyte to slow down the dissolution of manganese-based materials in the cycle.[13] These problems have seriously affected the potential of manganese-based materials as ZIB cathode materials. Therefore, these issues must be resolved before considering the use of manganese-based materials for viable ZIB cathode materials.

As a method to improve the physical and chemical properties of materials, defect engineering has been widely used in the modification of battery materials to improve the electrochemical performance of materials,[14] and manganese-based materials are no exception. Among the various defect engineering strategies that have been implemented, oxygen vacancies and cation doping may be the most reported.[15] Zhong *et al.* prepared anoxic δ-MnO_2 by the room temperature precipitation method and also reported that MnO_2 with oxygen vacancies was generated by reducing the crystallized manganese dioxide with NaBH4 solution.[16] The Gibbs free energy of Zn^{2+} adsorption near the oxygen vacancy can be reduced to thermal neutrality. This indicates that the adsorption/desorption process of Zn^{2+} on anoxic manganese dioxide is more reversible than the original manganese dioxide. In addition, since fewer electrons are required for Zn–O bonding in oxygen-deficient manganese dioxide, more valence electrons can be contributed to the delocalized electron cloud of the material, which helps increase the electrochemical capacity. Han *et al.* used density functional theory calculations and experimental results to study the effect of oxygen vacancies on β-MnO_2 dioxide.[17] Density functional theory calculations show that the main structure of β-MnO_2 prefers H^+ insertion rather than Zn^{2+}, and the introduction of oxygen defects will promote H^+ insertion into β-MnO_2. Doping with cations in manganese dioxide can release the

School of Mechanical and Electrical Engineering, Nanchang University, Nanchang 330031, China. E-mail: caoming@ncu.edu.cn

† Electronic supplementary information (ESI) available. See DOI: 10.1039/d1ra05775h

electrochemical activity potential of manganese-based oxides. Zhong *et al.* reported that cobalt-modified δ-MnO_2 nanosheets exhibited admirable self-healing behavior when used as a positive electrode.[18] The cobalt-containing material is well dispersed and can be used as the required active site to improve the charge transfer kinetics. Zhao *et al.* reported that the nickel-doped manganese dioxide prepared by the hydrothermal method, MnO_2 will undergo tetragonal distortion during discharge to promote H^+ transmission, and nickel doping aggravates the tetragonal distortion, thereby promoting α-MnO_2 Hydrogen bond formation and proton transport in manganese oxide.[19]

Defect engineering strategies have been widely studied, but there is only one specific defect in the above-mentioned research, and there are few reports on the combination of different defect engineering strategies. Therefore, in addition to simply adopting a single strategy, a combination of manufacturing different defect engineering strategies on materials can be implemented as a potential performance improvement method for the modification of the cathode manganese-based oxides of ZIBs. In order to further study the impact of defect engineering on materials, as a supplement to the implementation of the defect engineering strategy combination, in this study, nickel-doped α-MnO_2 nanowires were prepared by a simple hydrothermal method and MnO_2 was further processed with $NaBH_4$. For the first time, a cathode material with composite defects of cation doping and oxygen vacancies was obtained.

Experimental section

Preparation of Ni-doped α-MnO_2 nanowires

Dissolve 0.948 g $KMnO_4$ (0.006 mol) and 0.406 g $MnSO_4 \cdot H_2O$ (0.0024 mol) with $NiCl_2 \cdot 6H_2O$ with different Mn and Ni ratios in 60 ml deionized water, magnetically stirred for 30 minutes, the mixed solution was transferred to a 100 ml autoclave lined with tetrafluoroethylene and heated at 160 °C for 12 hours. The obtained precipitate was collected, washed and filtered three times with deionized water and absolute ethanol, and finally dried in an oven at 80 °C for 12 hours to obtain Ni-doped α-MnO_2 nanowires (denoted as KNMO). The original α-MnO_2 is obtained under similar conditions and is denoted as KMO.

Preparation of α-MnO_2 nanowires with oxygen vacancy and composite defects

0.087 g of KMO and KNMO (0.001 mol) were slowly added to 50 ml of $NaBH_4$ solution (1mol L^{-1}), stirred for 3 hours, then aged for 1 hour, and collected The precipitate obtained was washed and filtered three times with deionized water and absolute ethanol, and finally dried in an oven at 80 °C for 12 hours to obtain α-MnO_2 nanowires with oxygen vacancy and composite defects (denoted as d-KMO and d-KNMO).

Characterization

The composition of the sample was identified by X-ray diffraction (XRD) equipment (Bruker D8 ADVANCE diffractometer). The element composition and valence state of the sample were identified by X-ray photoelectron spectroscopy (XPS, ESCALA-B25OXi). The inductively coupled plasma optical emission spectrometer (ICP-OES, Agilent5100VDV) analyze the specific element ratios, and use Renishaw INVIA for Raman spectroscopy. Scanning electron microscopes (SEM, FEI Quanta 200FEG) were used to observe the micro morphology of the samples. The crystal plane and element distribution are characterized by a transmission electron microscope (TEM, JEOL JEM2100F), the specific surface area of the sample was measured by Micromeritics ASAP 2920 Surface Area and Porosity Analyzer.

Electrochemical measurements

The prepared manganese dioxide nanowires, carbon black and polyvinylidene fluoride were mixed in a mass ratio of 7 : 2 : 1, and an appropriate amount of *N*-methyl-2-pyrrolidone (NMP) was added dropwise. The slurry was obtained after manual grinding in a mortar for 20 minutes. Then, the slurry was uniformly coated on a stainless steel mesh current collector and dried in an oven at 80 °C for 8 hours to obtain a cathode piece. Zinc foil and glass fiber were used as the anode and separator, respectively, and 2 M $ZnSO_4$ and 0.1 M $MnSO_4$ solution was employed as the electrolyte. The above materials were used to assemble CR2032 coin cell in air to measure the electrochemical performance. After the assembled battery was allowed to stand at room temperature for 24 hours, the galvanostatic charge/discharge curves of the batteries was measured on the Neware Battery Test System (BTS-4000), the measured voltage was 1.0–1.8 V and cyclic voltammetry test and electrochemical impedance spectroscopy (EIS) test of the battery was carried out on the CHI660E electrochemical workstation. EIS test was performed with an AC amplitude of 5 mV over the frequency ranging from 10^5 Hz to 0.01 Hz.

Results and discussion

The stoichiometry of samples with different types of defects were analyzed by inductively coupled plasma optical emission spectrometer (ICP-OES). The sample detected K element. The result confirmed that the stoichiometry of the original sample without Ni^{2+} was $K_{0.127}MnO_2$ (KMO) and the stoichiometry of the less Ni-doped sample was $K_{0.109}Ni_{0.03}1Mn_{0.969}O_2$ (0.4KNMO), and the typical stoichiometry of Ni^{2+} doped MnO_2 was $K_{0.100}Ni_{0.077}Mn_{0.923}O_2$ (KNMO), and the stoichiometry of Ni^{2+} doped and oxygen vacancy composite defect engineering modified MnO2 was $K_{0.078}Ni_{0.090}Mn_{0.910}O_2$ (d-KNMO). The specific atomic ratio was shown in Table S1.† The sample contains about 10% K^+, and K^+ is likely to be embedded in the tunnel to stabilize the structure.

The crystal phase of the sample was detected by X-ray diffraction (XRD) as shown in the Fig. 1a and S1d.† The X-ray diffraction patterns of all samples showed several characteristic peaks of MnO_2. The main peaks at 18.1, 28.8, and 37.5° correspond to the (200), (310) and (211) crystal planes of MnO_2, respectively, indicating the main components of these samples

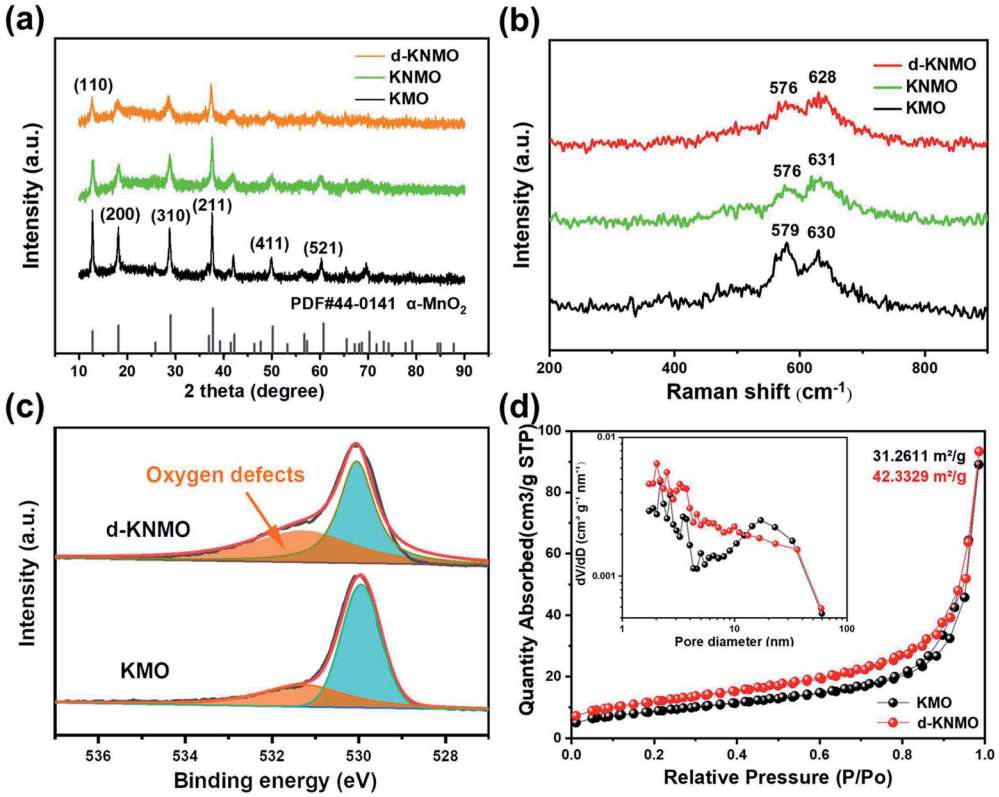

Fig. 1 Structural characterization of MnO_2 with different defects (a) Comparison of XRD patterns of KMO, KNMO and d-KNMO (b) Raman spectra of KMO, KNMO and d-KNMO (c) O1s XPS spectra of KMO and d-KNMO (d) nitrogen of KMO and d-KNMO adsorption–desorption curves.

are all α-MnO_2 belonging to the tetragonal crystal system, and the space group is $I4/m(87)$. In addition, in the MnO_2 samples doped with nickel ions, lack of oxygen and composite defects, except for the characteristic peaks of α-MnO_2, no obvious impurity peaks were found. Compared with KMO, the broad and weak characteristic peaks of KNMO indicated that KNMO has the general characteristics of poor crystallinity. The comparison of 0.4KNMO and KNMO shows that this trend is intensified with the increase of nickel ions. After KNMO was modified by oxygen vacancy (d-KNMO), this feature was further enhanced. This shows that the two-step method to form defects is effective.

The Raman spectra of KMO, KNMO and d-KNMO are shown in the Fig. 1b. KMO has Raman bands at 579 cm^{-1} and 630 cm^{-1}, which correspond to the ν_5(Mn–O) and ν_6(Mn–O) stretching vibration of the MnO_6 group, respectively.[20] Compared with KMO, the intensity of the vibration peaks of d-KNMO has decreased, and the ν_5 and ν_6 bands shift to lower wavenumbers. This may be due to the reduction of manganese–oxygen bonds caused by cation ion doping and the introduction of oxygen defects.

In addition, the existence of oxygen vacancies was verified by X-ray photoelectron spectroscopy (XPS) as shown in the Fig. 1c. The peaks of KMO and d-KNMO at 530 eV are originate from the widespread lattice oxygen in metal compounds. And the peak at 531.3 eV is attributed to oxygen vacancies.[17] It is obvious that the oxygen vacancy peak in d-KNMO has a higher peak intensity and a larger integration area. This phenomenon proves that there are more oxygen vacancies in the crystal structure of d-KNMO than in KMO.

The electrochemical performance of MnO_2 material is closely related to its ability to adsorb ions, that is, the micropore parameters, so the nitrogen adsorption and desorption isotherms of KMO and d-KNMO was experimentally studied. Compared with KMO, d-KNMO has type IV gas adsorption isotherm and H3 hysteresis loop, which shows that MnO_2 material has typical mesoporous characteristics.[21] The specific surface areas of d-KNMO is 42.3329 $m^2\ g^{-1}$, which is about 35.4% higher than the specific surface area of KMO (31.2611 $m^2\ g^{-1}$). It can be seen that the influence of doping elements and oxygen vacancies on the specific surface area is significant, and it also contributes to the enhancement of electrochemical performance. The pore size distribution range is 1.7–300 nm, the average pore size is 17.0854 nm and 14.1441 nm, and the total pore volume is 0.069515 and 0.073647 $cm^3\ g^{-1}$, respectively. The pore size distribution shows that the pores of d-KNMO are more distributed in the small pore area. The measurement result also proves that Ni doping and oxygen vacancies did not destroy the mesoporous structure of MnO_2, which is consistent with the results of SEM and TEM observations. The mesoporous structure is conducive to the full contact and efficient penetration of the electrolyte into the nanowires, and promotes the rapid transmission of zinc ions and protons.

In order to further understand the microstructure and element distribution of KMO and d-KNMO, scanning electron microscopy (SEM) and transmission electron microscopy (TEM) observations were performed on the materials as shown in Fig. 2 and S1.† The SEM images of Fig. 2a and d show that the prepared MnO_2 sample has a one-dimensional nanowire structure with well-dispersed and uniform wire diameter. The diameter of the nanowire is about 70 nm. The MnO_2 with composite defects presents the morphology of nanorods. It becomes shorter and smaller in volume, which is beneficial to increase the specific surface area of MnO_2. This is verified in the BET test results. The TEM images are consistent with the SEM results, and α-MnO_2 exhibits a uniform nanowire microstructure. The high-resolution transmission electron microscopy (HRTEM) images of Fig. 2b and e show clear lattice fringes of KMO and d-KNMO, and the lattice spacing corresponding to the (310) crystal plane is 3.24 Å and 3.20 Å, respectively. The lattice spacing in Fig. S3† is 4.83 Å and 4.76 Å, respectively, corresponding to (200) crystal planes. There is a slight difference in the crystal plane spacing between the two samples, which is consistent with previous reports on ion doping and oxygen defects.[16,19] Compared with KMO, the d-KNMO sample shows more dark small pits and the surface is rougher, which may be caused by oxygen vacancies. The selected-area electron diffraction (SAED) observation results of the samples showed that both samples formed good symmetric and ordered single crystals, and the diffraction pattern showed diffraction spots on the (200) crystal plane. In addition, the element distribution of d-KNMO was analyzed through the element mapping as shown in the Fig. 2g, the results proved the uniform distribution of Mn, K, and Ni in the sample.

To explore the effects of composite defects with cation doping and oxygen vacancy on the electrochemical performance of α-MnO_2, coin cell was used with KMO and d-KNMO as cathode, zinc foil as anode and 2 M $ZnSO_4$ + 0.1 M $MnSO_4$ solution as the electrolyte for electrochemical testing as shown in Fig. 3. The cyclic voltammetry (CV) curve shows that KMO has two reduction peaks at 1.18 V and 1.31 V, and an oxidation peak at 1.61 V. d-KNMO has two reversible redox peaks. Obvious cathodic peaks of d-KNMO can be observed at 1.19 V and 1.35 V, corresponding to the insertion of H^+/Zn^{2+} into the α-MnO_2 tunnel and the reduction of Mn^{4+} to a lower oxidation state (Mn^{3+}). During the anode scanning process, two anode peaks were observed at 1.61 and 1.65 V, respectively corresponding to the extraction of H^+/Zn^{2+} from the MnO_2 tunnel and the oxidation of Mn^{3+} to Mn^{4+}.[22] It is worth noting that the insertion potential of the d-KNMO cathode is higher than the insertion potential of the KMO cathode, indicating that the cation doping and oxygen vacancy are beneficial to the insertion of H^+ and Zn^{2+}. Compared with KMO, the d-KNMO electrode shows higher peak intensity and larger CV curve integral area, indicating that the electrochemical performance of the MnO_2 electrode under the action of composite defects has been significantly improved.

The specific capacity graphs at different current densities show the rate performances of pure MnO_2 and composite defects materials as shown in Fig. 3b. The discharge capacity of KMO at current densities of 0.1, 0.2, 0.3, 0.5, 1, and 2 A g^{-1} are

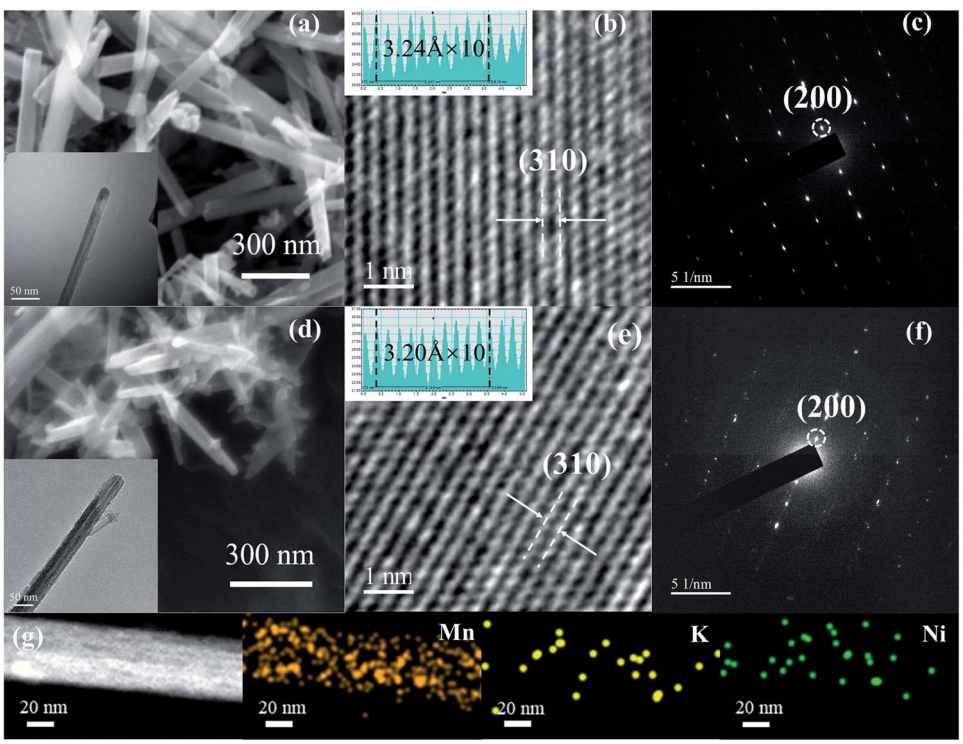

Fig. 2 Micro morphology and structure of KMO and d-KNMO (a and d) SEM and TEM images of KMO and d-KNMO (b and e) HRTEM images of KMO and d-KNMO (c and f) The corresponding SAED spectra (g) shows the mapping results of Mn, K, and Ni.

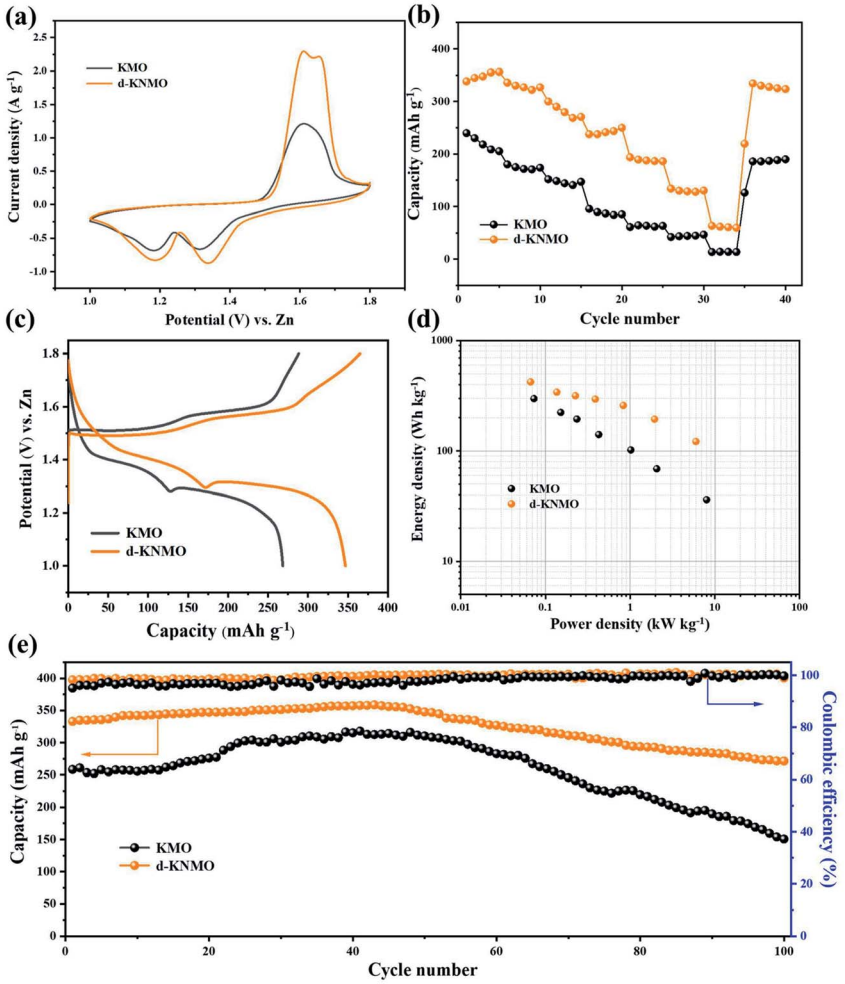

Fig. 3 The electrochemical performance of KMO and d-KNMO (a) cyclic voltammetry curves at a scan rate of 0.5 mV s^{-1} (b) rate performances (c) galvanostatic charge/discharge curves at a current density of 0.1 A g^{-1} (d) the Ragone plots (e) cycling performances and corresponding coulombic efficiencies at current densities of 0.1 A g^{-1}.

240.2, 180.1, 151.7, 95.5, 61.3, 42.1 mA h g^{-1}, and the discharge capacity of d-KNMO with composite defects can reach 342.3, 335.7, 300.0, 237.7, 193.7, 133.9 mA h g^{-1}. Surprisingly, the capacity of d-KNMO can still reach 63.6 mA h g^{-1} at a high current density of 5 A g^{-1}. It is much higher than 13.5 mA h g^{-1} of KMO. At the end of the rate test, the current density of 0.1 A g^{-1} was used for cycling again. d-KNMO still has a specific discharge capacity of 338.2 mA h g^{-1}, which is 98.8% of the initial discharge value, which is better than the capacity retention rate of KMO (77.3%).

The galvanostatic charge/discharge (GCD) curves show the capacities of the three materials as shown in Fig. 3c. When the current density is 0.1 A g^{-1}, d-KNMO can reach an astonishing specific capacity of 346 mA h g^{-1}. Under the same conditions, KMO only has a low specific capacity of 268 mA h g^{-1}. The curve shows a clear turning point at about 1.3 V, indicating that the storage mechanism has changed during the discharge process (Fig. 2c), corresponding to the insertion of different ions (H^+ and Zn^{2+}).[23] The superior performance of d-KNMO can be further obtained from the Ragone plots in the Fig. 2d. d-KNMO can provide a maximum energy density of 422 W h kg^{-1} (based on the mass of the cathode active material), which was better than that of KMO (298 W h kg^{-1}). While the maximum power density is up to 6 kW kg^{-1}, the energy density can still reach 121 W h kg^{-1}.

In order to evaluate the long-term cycling stability of the material, KMO and d-KNMO were cycled at a low current density of 0.1 A g^{-1} as shown in Fig. 3e. After 100 cycles, the remaining capacity of d-KNMO is 277.1 mA h g^{-1} and the capacity retention rate of d-KNMO was 81.5%, which was better than 58.3% of KMO, indicating that d-KNMO with composite defects has excellent cycle life. In order to further prove that composite defects improve the cycle performance of the material, d-KNMO was cycled at a high current density of 2 A g^{-1} as shown in Fig. S3.† After 1000 cycles, the coulombic efficiency (CE) was about 100%, and the capacity retention rate reached 57.4% which was much higher than the capacity retention rate of KMO (20.0%).

When testing the long-term cycle performance of the material, it was found that the specific capacity decreased after 40

cycles. Therefore, the samples after 40 cycles and 100 cycles were characterized to explore the reasons for the decrease in capacity. Fig. 4 shows the scanning electron micrographs and XRD patterns of *t* sample after 40 cycles and 100 cycles. Compared with unused α-MnO_2, the uniform wire diameter microstructure is destroyed after the cycle, and a new granular phase is formed on the surface of the nanowire. This phenomenon is aggravated with the increase of the cycle. A new diffraction peak appears in the XRD spectrum (Fig. 4c) after the sample is cycled. After comparison, it is found that it belongs to $ZnSO_4 \cdot 3Zn(OH)_2 \cdot 5H_2O$ (BZSP), which indicates that the energy storage mechanism of α-MnO_2 may be Combined Intercalation and Conversion Reaction Mechanism.[24] Zn^{2+} intercalation occurred during the discharge process, a chemical conversion reaction occurred as the discharge progressed and the by-product BZSP was generated. After intercalation and chemical conversion reaction, the morphological change of α-MnO_2 and the BZSP generated on the surface increase the resistance of further reaction, which are the reasons for the capacity decay.

Defect engineering can also improve the electrical conductivity of the material, thereby improving the electrochemical performance, so the electrochemical impedance spectroscopy (EIS) of the material was tested to get more information about the resistance and conductivity (Fig. S4†). In the curves of KMO and d-KNMO, the semicircle in the high frequency region corresponds to the internal resistance (R_S) and the charge transfer resistance (R_{CT}), and the oblique line in the low frequency region is attributed to the Warburg impedance (Z_W).[25] The semicircle in the high frequency region of d-KNMO is smaller, indicating that its R_S and R_{CT} are smaller, and the comparison of the diffuser tail also indicates that its Z_W is smaller.

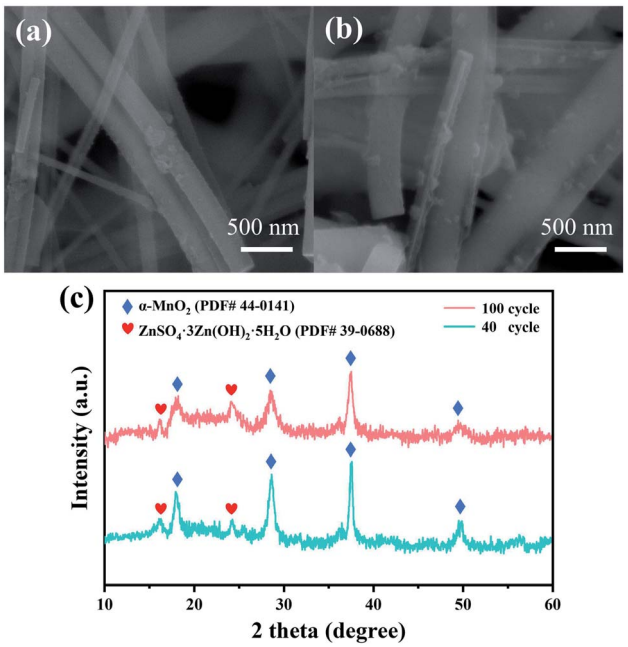

Fig. 4 Characterization of samples after cycling (40 and 100) (a and b) the scanning electron micrographs of samples after 40 cycles and 100 cycles (c) the corresponding X-ray diffraction patterns of samples.

At the same time, perform CV test on d-KNMO at different scan rates, as shown in the Fig. S5c and d. †The peak current has the following relationship with the scan rate:[26,27]

$$i = av^b$$

which can be expressed as

$$\log(i) = b\log(v) + \log(a).$$

By fitting the straight line of log(*i*) and log(*v*), the slope or *b* value can be obtained. When the value of *b* is 0.5, ion diffusion is dominant in the charge and discharge process. When the value of *b* is 1, the surface capacitance is dominant in the electrochemical process. The fitting calculation results show that the *b* values of peak 1, peak 2, and peak 3 are 0.60, 0.49, and 0.87, respectively, which indicates that the electrochemical process of the zinc ion battery in the experiment is a combination of ion diffusion and surface capacitance effects. For Zn/KMO as shown in the Fig. S5a and b,† the electrochemical process is also caused by ion diffusion and surface capacitance effects. By fitting a straight line of log(*i*) and log(*v*), the *b* values of peak 1, peak 2, and peak 3 are 0.65, 0.70, and 0.51, respectively.

In addition, in order to prove that the high capacity of d-KNMO is the result of the combined effect of nickel doping and oxygen vacancies, the electrochemical performance tests of single defect engineering materials were also carried out in the experiment as shown in the Fig. S6 and S7.† Through the comparison of the CV curves of KMO and KNMO, the half-width of the anode of KNMO was narrower than that of KMO, indicating that ion doping has caused the depolarization of the cathode and the diffusion kinetics of carriers may have changed, while d-KMO electrode showed higher peak intensity and larger integrated area of the CV curve, indicating that the capacity of the d-KMO electrode may be higher than that of the KNMO. The galvanostatic charge/discharge (GCD) test carried out afterwards proved this point. At a current density of 0.1 A g^{-1}, the first charge–discharge specific capacity of ion-doped KNMO is 292.5 mA h g^{-1} and d-KMO reaches 312.8 mA h g^{-1}. It is worth noting that the additional capacity (78 mA h g^{-1}) generated by the modification of composite defects is more than the additional capacity of the two single defects (69.3 mA h g^{-1}), which suggests that there is a synergistic effect between cation doping and oxygen vacancies. Not only that, d-KMO also has better rate performance and cycle performance than KNMO. The discharge capacities of KNMO at current densities of 0.1, 0.2, 0.3, 0.5, 1, 2 and 5 A g^{-1} were 290.7, 279.3, 249.6, 208.2, 129.1, 54.8 and 22.2 mA h g^{-1}, respectively, while the capacity of d-KMO were 315.3, 290.6, 246.8, 231.5, 194.0, 133.8 and 66.7 mA h g^{-1}. KNMO and d-KMO are cycled at a low current density of 0.1 A g^{-1}. After 100 cycles, the remaining capacity of d-KMO was 244.4 mA h g^{-1} and the capacity retention rate was 78.1%, which was better than 71.3% of KNMO. The supplementary experiment shows that compared with cation doping, the implementation of oxygen vacancy

strategy may be a more effective defect engineering to increase the capacity of zinc-ion batteries.

Nickel ion doping increases the specific capacity of α-MnO_2 not because nickel ions have redox activity and introduce additional insertion sites, but because nickel ions aggravate the lattice distortion in MnO_2 discharge and promote the diffusion and diffusion of H^+ transmission. Ion doping significantly improves the transfer kinetics of carriers, so that MnO_2 obtains a higher capacity. The oxygen vacancies obtained by NaBH4 reduction are embedded in the MnO_2 lattice and weaken the chemical bond between zinc and oxygen, reducing the electrons that zinc contributes to the formation of chemical bonds, so more valence electrons can be used in the charge and discharge process, and oxygen vacancies are conducive to achieving the high reversibility of carrier insertion/extraction, thereby increasing the specific capacity of the material.

Conclusions

In short, MnO_2 with composite defects of cation doping and oxygen vacancy was synthesized for the first time in the experiment, and the maximum capacity of 346 mA h g^{-1} was obtained at a current density of 0.1 A g^{-1} and the cycle performance was 40% higher than that of untreated MnO_2, the rate performance was also significantly improved, and the comparison of the performance of single defect engineering materials shows that oxygen vacancies may be a more effective defect engineering strategy than cation doping. The successful implementation of composite defects inspired us to combine other different defect engineering strategies (such as cation vacancies and anion doping), which provides new ideas for the modification of cathode materials.

Conflicts of interest

There are no conflicts to declare.

Acknowledgements

This research was supported by the National Natural Science Foundation of China (No. 51762034).

References

1 H. Lund, *Energy*, 2007, **32**, 912–919.
2 J. B. Goodenough and K.-S. Park, *J. Am. Chem. Soc.*, 2013, **135**, 1167–1176.
3 P. Wang, Y. Y. Ren, R. T. Wang, P. Zhang, M. J. Ding, C. X. Li, D. Y. Zhao, Z. Qian, Z. W. Zhang, L. Y. Zhang and L. W. Yin, *Nat. Commun.*, 2020, **11**, 1576.
4 J. H. Sun, M. Sadd, P. Edenborg, H. Gronbeck, P. H. Thiesen, Z. Y. Xia, V. Quintano, R. Qiu, A. Matic and V. Palermo, *Sci. Adv.*, 2021, **7**, eabf0812.
5 L. Wang, B. Zhang, B. Wang, S. Y. Zeng, M. W. Zhao, X. P. Sun, Y. J. Zhai and L. Q. Xu, *Angew. Chem., Int. Ed.*, 2021, **60**, 15381–15389.
6 D. L. Chao, W. H. Zhou, F. X. Xie, C. Ye, H. Li, M. Jaroniec and S. Z. Qiao, *Sci. Adv.*, 2020, **6**, 19.
7 X. Jia, C. Liu, Z. G. Neale, J. Yang and G. Cao, *Chem. Rev.*, 2020, **120**, 7795–7866.
8 X. Liu, J. Yi, K. Wu, Y. Jiang, Y. Liu, B. Zhao, W. Li and J. Zhang, *Nanotechnology*, 2020, **31**, 122001.
9 F. Wan and Z. Niu, *Angew. Chem., Int. Ed.*, 2019, **58**, 16358–16367.
10 G. Zampardi and F. La Mantia, *Curr. Opin. Electrochem.*, 2020, **21**, 84–92.
11 W. Xu, C. Sun, K. Zhao, X. Cheng, S. Rawal, Y. Xu and Y. Wang, *Energy Storage Materials*, 2019, **16**, 527–534.
12 M. H. Alfaruqi, S. Islam, D. Y. Putro, V. Mathew, S. Kim, J. Jo, S. Kim, Y.-K. Sun, K. Kim and J. Kim, *Electrochim. Acta*, 2018, **276**, 1–11.
13 C. Qiu, X. Zhu, L. Xue, M. Ni, Y. Zhao, B. Liu and H. Xia, *Electrochim. Acta*, 2020, **351**, 136445.
14 Y. H. Tian, X. Z. Liu, L. Xu, D. Yuan, Y. H. Dou, J. X. Qiu, H. N. Li, J. M. Ma, Y. Wang, D. Su and S. Q. Zhang, *Adv. Funct. Mater.*, 2021, **31**, 2101239.
15 T. Xiong, Y. Zhang, W. S. V. Lee and J. Xue, *Adv. Energy Mater.*, 2020, **10**, 2001769.
16 T. Xiong, Z. G. Yu, H. Wu, Y. Du, Q. Xie, J. Chen, Y. W. Zhang, S. J. Pennycook, W. S. V. Lee and J. Xue, *Adv. Energy Mater.*, 2019, **9**, 1803815.
17 M. Han, J. Huang, S. Liang, L. Shan, X. Xie, Z. Yi, Y. Wang, S. Guo and J. Zhou, *iScience*, 2020, **23**, 100797.
18 Y. J. Zhong, X. M. Xu, J. P. Veder and Z. P. Shao, *Iscience*, 2020, **23**, 28.
19 Q. Zhao, A. Song, W. Zhao, R. Qin, S. Ding, X. Chen, Y. Song, L. Yang, H. Lin, S. Li and F. Pan, *Angew. Chem., Int. Ed. Engl.*, 2020, **60**, 4169–4174.
20 C. M. Julien, M. Massot and C. Poinsignon, *Spectrochim. Acta, Part A*, 2004, **60**, 689–700.
21 S. Xin, Y. G. Guo and L. J. Wan, *Acc. Chem. Res.*, 2012, **45**, 1759–1769.
22 M. H. Alfaruqi, J. Gim, S. Kim, J. Song, P. Duong Tung, J. Jo, Z. Xiu, V. Mathew and J. Kim, *Electrochem. Commun.*, 2015, **60**, 121–125.
23 G. Fang, J. Zhou, A. Pan and S. Liang, *ACS Energy Lett.*, 2018, **3**, 2480–2501.
24 Y. F. Huang, J. Mou, W. B. Liu, X. L. Wang, L. B. Dong, F. Y. Kang and C. J. Xu, *Nano-Micro Lett.*, 2019, **11**, 49.
25 S. Rodrigues, N. Munichandraiah and A. K. Shukla, *J. Power Sources*, 2000, **87**, 12–20.
26 K. Zhang, M. H. Park, L. M. Zhou, G. H. Lee, W. J. Li, Y. M. Kang and J. Chen, *Adv. Funct. Mater.*, 2016, **26**, 6728–6735.
27 D. L. Chao, C. R. Zhu, P. H. Yang, X. H. Xia, J. L. Liu, J. Wang, X. F. Fan, S. V. Savilov, J. Y. Lin, H. J. Fan and Z. X. Shen, *Nat. Commun.*, 2016, **7**, 12122.